

See discussions, stats, and author profiles for this publication at: <https://www.researchgate.net/publication/11174589>

Intramolecular Dynamics of Low Molecular Weight Protein Tyrosine Phosphatase in Monomer–Dimer Equilibrium Studied by NMR: A Model for Changes in Dynamics upon Target Binding

ARTICLE *in* JOURNAL OF MOLECULAR BIOLOGY · OCTOBER 2002

Impact Factor: 4.33 · DOI: 10.1016/S0022-2836(02)00714-3 · Source: PubMed

CITATIONS

41

READS

6

4 AUTHORS, INCLUDING:



Tomas Åkerud

AstraZeneca

7 PUBLICATIONS 168 CITATIONS

SEE PROFILE



Mikael Akke

Lund University

102 PUBLICATIONS 5,451 CITATIONS

SEE PROFILE

Intramolecular Dynamics of Low Molecular Weight Protein Tyrosine Phosphatase in Monomer–Dimer Equilibrium Studied by NMR: A Model for Changes in Dynamics upon Target Binding

Tomas Åkerud^{1,2}, Eva Thulin¹, Robert L. Van Etten³ and Mikael Akke^{1*}

¹Department of Biophysical Chemistry, Lund University
Box 124, SE-221 00 Lund
Sweden

²Structural Chemistry
Biovitrum, Stockholm, Sweden

³Department of Chemistry
Purdue University, West
Lafayette, IN, USA

Low molecular weight protein tyrosine phosphatase (LMW-PTP) dimerizes in the phosphate-bound state in solution with a dissociation constant of $K_d = 1.5(\pm 0.1)$ mM and an off-rate on the order of 10^4 s⁻¹. ¹H and ¹⁵N NMR chemical shifts identify the dimer interface, which is in excellent agreement with that observed in the crystal structure of the dimeric S19A mutant. Two tyrosine residues of each molecule interact with the active site of the other molecule, implying that the dimer may be taken as a model for a complex between LMW-PTP and a target protein. ¹⁵N relaxation rates for the monomeric and dimeric states were extrapolated from relaxation data acquired at four different protein concentrations. Relaxation data of satisfactory precision were extracted for the monomer, enabling model-free analyses of backbone fluctuations on pico- to nanosecond time scales. The dimer relaxation data are of lower quality due to extrapolation errors and the possible presence of higher-order oligomers at higher concentrations. A qualitative comparison of order parameters in the monomeric and apparent dimeric states shows that loops forming the dimer interface become rigidified upon dimerization. Qualitative information on monomer–dimer exchange and intramolecular conformational exchange was obtained from the concentration dependence of auto- and cross-correlated relaxation rates. The loop containing the catalytically important Asp129 fluctuates between different conformations in both the monomeric and dimeric (target bound) states. The exchange rate compares rather well with that of the catalyzed reaction step, supporting existing hypotheses that catalysis and enzyme dynamics may be coupled. The side-chain of Trp49, which is important for substrate specificity, exhibits conformational dynamics in the monomer that are largely quenched upon formation of the dimer, suggesting that binding is associated with the selection of a single side-chain conformer.

© 2002 Elsevier Science Ltd. All rights reserved

Keywords: conformational exchange; dimerization; enzyme dynamics; order parameters; rotational diffusion tensor

*Corresponding author

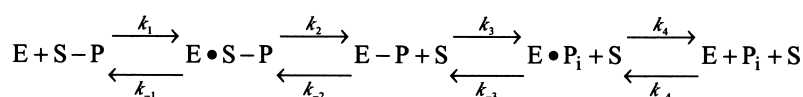
Introduction

Phosphorylation of tyrosine side-chains in proteins constitutes an essential mechanism of

intracellular signal transduction regulating cell growth, proliferation and differentiation.^{1,2} Protein phosphorylation is controlled by the enzymatic actions of kinases and phosphatases that phosphorylate and dephosphorylate target proteins, respectively. A thorough understanding of phosphatase activity on the molecular level requires detailed characterization of the changes in structure and dynamics of each of the interacting molecules at each step of the catalytic cycle. Low molecular weight protein tyrosine phosphatases (LMW-PTPs) are excellent candidates for studying

Abbreviations used: HSQC, heteronuclear single quantum coherence; LMW-PTP, low molecular weight protein tyrosine phosphatase; NOE, nuclear Overhauser effect; NOESY, NOE spectroscopy; P-loop, phosphate-binding loop.

E-mail address of the corresponding author: mikael.akke@bpc.lu.se



Scheme 1.

phosphatase activity, since they are small cytosolic proteins ($M_r \sim 18$ kDa) that consist of a single stable domain ($t_m \sim 70^\circ\text{C}$).^{3,4} Except for the common signature motif of the phosphate binding loop (P-loop) CXXXXXR(S/T), LMW-PTPs exhibit no significant sequence similarity to other classes of protein tyrosine phosphatases (PTPs). However, all PTPs include a conserved aspartic acid residue that is catalytically important as a general acid in the reaction mechanism.^{5,6} The basic reaction path involves: (1) binding of substrate; (2) transfer of phosphate from tyrosine on the protein substrate to the nucleophilic cysteine (Cys12 in bovine LMW-PTP); (3) dephosphorylation of the phosphoenzyme intermediate; and (4) release of the inorganic phosphate from the enzyme (Scheme 1).⁶

The aspartic acid is involved in step 2 and (for some PTPs) step 3. In LMW-PTP, the aspartic acid is located in a long, extended loop segment (here denoted the D-loop). In high molecular weight PTPs, the corresponding loop has been observed in two distinct conformations: in the substrate bound state, the loop is “closed” over the active site, whereas in the free state the loop is “open” and located ~ 10 Å away from the active site.^{7–9} This conformational change can be described as a hinged loop movement, and is the only prominent structural difference between ligand-free and ligand-bound states. In the case of LMW-PTP, the open conformation of the D-loop has not been observed, because structures are available only for closed states with various compounds bound in the active site. However, in *Saccharomyces cerevisiae* LMW-PTP the D-loop is observed in slightly

different orientations in the phosphate- and substrate-bound states.¹⁰ It has been suggested that the conformational dynamics of the D-loop may be related to the catalytic activity of the protein.^{5,6,8} Amide hydrogen exchange measurements by mass spectrometry have established that the D-loop is flexible in the *Yersinia* PTP.¹¹ Additional results for the *Yersinia* PTP have been obtained by monitoring spectroscopic properties of a tryptophan side-chain, located near the catalytically important aspartate. Steady-state ultraviolet resonance Raman spectroscopy suggests that the D-loop exists in two equally populated conformations, closed and open, in the free state, but that the closed conformation predominates in the ligand-bound state.¹² Furthermore, time-resolved fluorescence anisotropy decay data have indicated that the transition rate between conformations is on the order of 10^8 s^{-1} ,¹² which is five orders of magnitude greater than the catalytic rate constant. In contrast, previous NMR studies of phosphate-bound LMW-PTP indicated that residues in the D-loop exhibit conformational exchange with a rate on the order of 10^3 s^{-1} ,¹³ which is close to the catalytic rate for this enzyme.¹⁴

LMW-PTP from bovine heart is one of the most extensively studied LMW-PTPs.¹⁵ Crystal structures of LMW-PTP have been reported with the leaving group phosphate,¹⁶ the substrate analog Hepes,¹⁶ and the transition state analog vanadate¹⁷ bound to the active site. To date, no structure has been published of the non-ligated form of LMW-PTP, or of any complex with a target peptide. However, a recent crystal structure of the phosphate-bound state of the S19A mutant of bovine LMW-PTP revealed a dimer, in which the side-chains of Tyr131 and Tyr132 of each molecule insert into the active site of the other molecule.¹⁸ Previous crystal structures were obtained with heterocyclic sulfonate inhibitors that occupy the active site, apparently preventing formation of dimers. The dissociation constant for the dimer in 0.1 M Tris buffer (pH 7.3) was estimated by equilibrium ultracentrifugation to fall in the range 1–5 mM for both the S19A mutant and wild-type protein.¹⁸ It has been reported that Tyr131 and Tyr132 can be phosphorylated *in vivo* by Src-, Lck- and Fyn-kinases, and that tyrosine phosphorylation is correlated with increased phosphatase activity.^{19,20} These observations have led to the hypothesis that the dimeric state of LMW-PTP may have an auto-regulating function.¹⁸ The weak association constant indicates that dimeric LMW-PTP can be of biological relevance only if the protein exists in high local concentrations in the cell. High effective concentrations of LMW-PTP could result if it accumulates near the intracellular

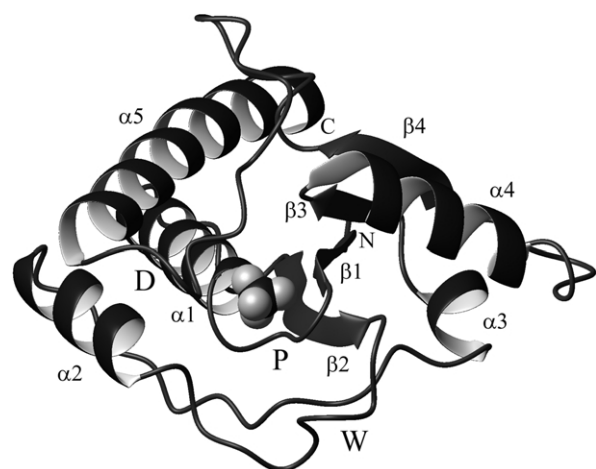


Figure 1. Ribbon diagram of the crystal structure of monomeric LMW-PTP (1PNT¹⁶). The locations of the P-, D-, and W-loops are indicated (D, P, W). The secondary structure elements are labeled $\alpha 1$ –5 and $\beta 1$ –4. The Figure was prepared using MOLMOL.⁶⁹

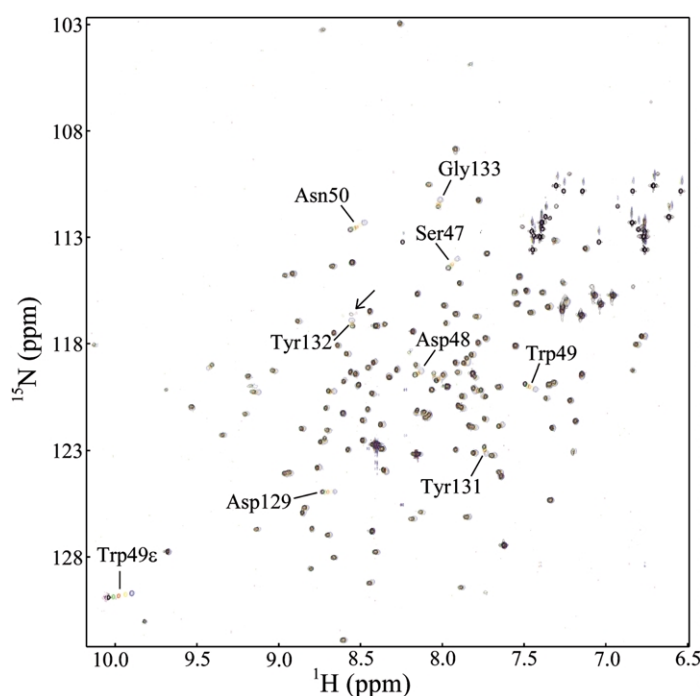


Figure 2. Superposition of ^{15}N -HSQC spectra of LMW-PTP acquired at six different concentrations ranging from 0.026 to 1.24 mM. Residues with the most pronounced shift changes are indicated. An arrow indicates the position of an unidentified peak (tentatively assigned to Ile127) that shows the largest concentration-dependent ^1H chemical shift change. Given the processing parameters used to produce the spectra shown here, this peak is visible only at the two lowest concentrations. The spectra are color-coded as follows: magenta, 0.026 mM; black, 0.079 mM; green, 0.17 mM; red, 0.34 mM; yellow, 0.66 mM; blue, 1.24 mM.

membrane, and/or interacts with target proteins in oligomeric assemblies. For example, LMW-PTP binds to the tetrameric form of the EphB1 receptor tyrosine kinase.²¹ It remains to be investigated how the dissociation constant varies with osmolyte concentration; possibly, dimerization may be significant in the cytosol as a consequence of macromolecular crowding.²² Notwithstanding the open questions regarding a functional role of the dimer, it may be taken as a generic model for a complex between LMW-PTP and a protein substrate.

The secondary structure of LMW-PTPs consists of five α -helices ($\alpha 1$ – $\alpha 5$) and four β -strands ($\beta 1$ – $\beta 4$) (see Figure 1). The β -strands form a highly twisted β -sheet. There are two $\beta\alpha\beta$ -motifs ($\beta 1$ – $\alpha 1$ – $\beta 2$ and $\beta 3$ – $\alpha 4$ – $\beta 4$). Two long and extended loop segments connect $\alpha 2$ with $\alpha 3$ and $\beta 4$ with $\alpha 5$. The active site is made up of three loop regions. The phosphate binding loop (the P-loop, residues 12–19) is located between $\beta 1$ and $\alpha 1$, and includes the nucleophile Cys12 and the catalytically important Arg18. The loop between $\beta 2$ and $\alpha 2$ (the W-loop, residues 46–56) is lining one side of the active site, and includes Trp49, Asn50 and Arg53, which control substrate specificity.^{23,24} The C-terminal part of the long and partly extended loop containing the catalytically critical²⁵ Asp129 (the D-loop, residues 116–134) is lining the other side of the active site.

The biological function of LMW-PTP has not yet been elucidated with certainty, but several proteins have been reported to interact with mammalian LMW-PTP *in vivo*. For example, human LMW-PTP binds to EphB1 (ELK) receptor complexes,²¹ and rat LMW-PTP associates with the insulin receptor β -subunit, thereby downregulating the mitogenic and metabolic insulin-mediated response in fibroblasts.²⁶ In mammalian tissues, LMW-PTP is often present in two isoforms, A and B, that differ

by alternative splicing of residues 40–73, a segment that includes the W-loop.^{27,28} The sequence differences between isoforms A and B result in different substrate specificities.^{23,24} Bovine heart LMW-PTP is 94% identical in sequence to human isoform B, and the two proteins show similar specific activities towards substrates.²⁴

Here we characterize the dimer interaction and the intramolecular dynamics of bovine LMW-PTP in monomer–dimer equilibrium using NMR spectroscopy. ^{15}N relaxation rates for the monomer and dimer were extracted from experiments performed at four different sample concentrations. The monomer represents the enzyme with non-covalently bound phosphate, i.e. the state between reaction steps 3 and 4 of Scheme 1, while the dimer can be considered a model for a complex between LMW-PTP and a target protein. The results provide quantitative information about the amplitudes of structural fluctuations on ps–ns time scales in the monomer, and qualitative differences in these quantities between the monomer and dimer. In addition, the global rotational diffusion properties of both the monomer and dimer were determined and compared to hydrodynamic models. The effect of dimer formation on intramolecular conformational exchange was monitored as the concentration dependence of the difference between auto- and cross-correlated transverse relaxation rates.

Results and Discussion

Chemical shift assignments

LMW-PTP consists of 157 amino acid residues, out of which five are proline residues that do not

give rise to cross-peaks in the ^1H - ^{15}N HSQC spectrum. Assignments for 95% of the backbone amide groups were obtained in the present experimental conditions, based on a NOESY-HSQC experiment with 100 ms mixing time, and assignments published for 30 °C and 100 mM sodium phosphate, pH 5.0 (94% complete),²⁹ together with assignments at 37 °C.¹³ Assignments that were previously missing for a subset of residues at 37 °C could be transferred from the assignments at 30 °C; these included Gly14, Val40, Lys123, and Leu125. The Lys123 cross-peak was very broadened, precluding detailed analysis. The chemical shifts of the indole side-chain NH groups of Trp39 and Trp49 were unambiguously assigned using the NOESY-HSQC spectrum. Identification of these resonances was important, because one of the most pronounced chemical shift changes in the dilution series is observed for the Trp49 indole side-chain proton resonance (see below).

Identification of the dimer interaction surface

Dimerization of LMW-PTP was investigated by following ^1H and ^{15}N chemical shift changes over a concentration range from 26 μM to 5 mM (see Figure 2). Significantly concentration-dependent chemical shifts were observed for a subset of residues: Ser47, Asp48, Trp49, Asn50, Asp129, Tyr131, Tyr132, and Gly133, which together form a contiguous region in the structure. The largest shift change in the ^1H dimension was observed for an unassigned cross-peak that was tentatively assigned to Ile27, because this is the only residue close to the dimer interface that remained unassigned. In the ^{15}N dimension, the largest shift change was observed for Ser47. The absolute values of the ^1H and ^{15}N chemical shift changes ranged between 0.10 and 0.26 ppm and 0.19–0.48 ppm, respectively. The chemical shift changes are mapped onto the crystal structure of the LMW-PTP S19A dimer in Figure 3. As can be seen, the interaction surface identified by the chemical shift changes agrees very well with that observed in the crystal structure. At concentrations above 1.5 mM, the shift changes level out faster than expected for a pure monomer–dimer equilibrium (data not shown). At concentrations above 2.5 mM, cross-peaks were severely broadened, and the sample became opaque after one hour at 37 °C. ^1H -line-broadening increases uniformly for all residues over the entire concentration range. In contrast, no additional chemical shift changes are observed except for those at the dimer interface. Together, these observations indicate non-specific interactions that lead to precipitation of the sample at high concentrations; similar effects have been reported for other proteins.³⁰ At concentrations below 1.5 mM, the shift changes follow the dependence expected for a monomer–dimer equilibrium, as shown in Figure 4, indicating that problems with non-specific higher-order aggregation are largely mitigated at these concentrations. Hence,

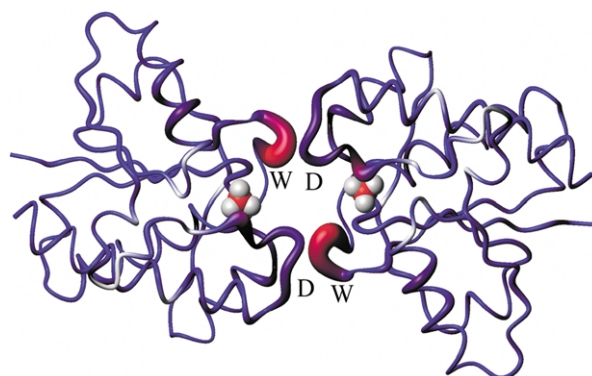


Figure 3. Concentration-dependent chemical shifts displayed on the dimeric crystal structure of the LMW-PTP S19A mutant (1C0E¹⁸). The sum of the chemical shift changes, in units of Hz, observed for the ^{15}N and ^1H nuclei of each residue, are encoded using both color and radius of the corresponding backbone tube segment. The range of chemical shift changes, 0–77 Hz, is represented by a continuous color scheme ranging from blue to red, and a radius ranging from 0.2 to 1.5 Å; white indicates unassigned residues and black indicates proline residues. The phosphate ions bound in the active sites are shown as space filling models. The Figure was prepared using MOLMOL.⁶⁹

we avoided working at concentrations above 1.5 mM. Pure monomer–dimer equilibrium was assumed at concentrations below 1.5 mM.

Determination of the dimer dissociation constant

The dissociation constant of the monomer–dimer equilibrium was determined from a dilution series of ^1H - ^{15}N HSQC spectra, acquired on six samples of well-determined concentrations

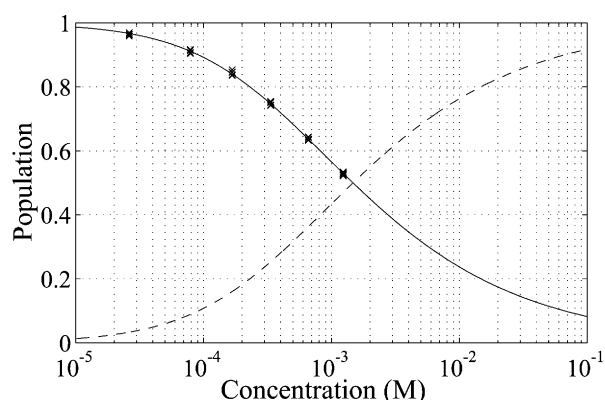


Figure 4. Populations corresponding to normalized concentration-dependent ^1H chemical shift changes for a monomer–dimer equilibrium model; $p_M = (\omega_{\text{obs}} - \omega_D) / (\omega_M - \omega_D)$, see equation (3). The symbols indicate the normalized experimental data points for each of the six resonances included in the fit of equation (4) to determine the dissociation constant. The continuous and broken lines indicate the fitted populations p_M and p_D , respectively. The graph was made using Grace (Grace Development Team).

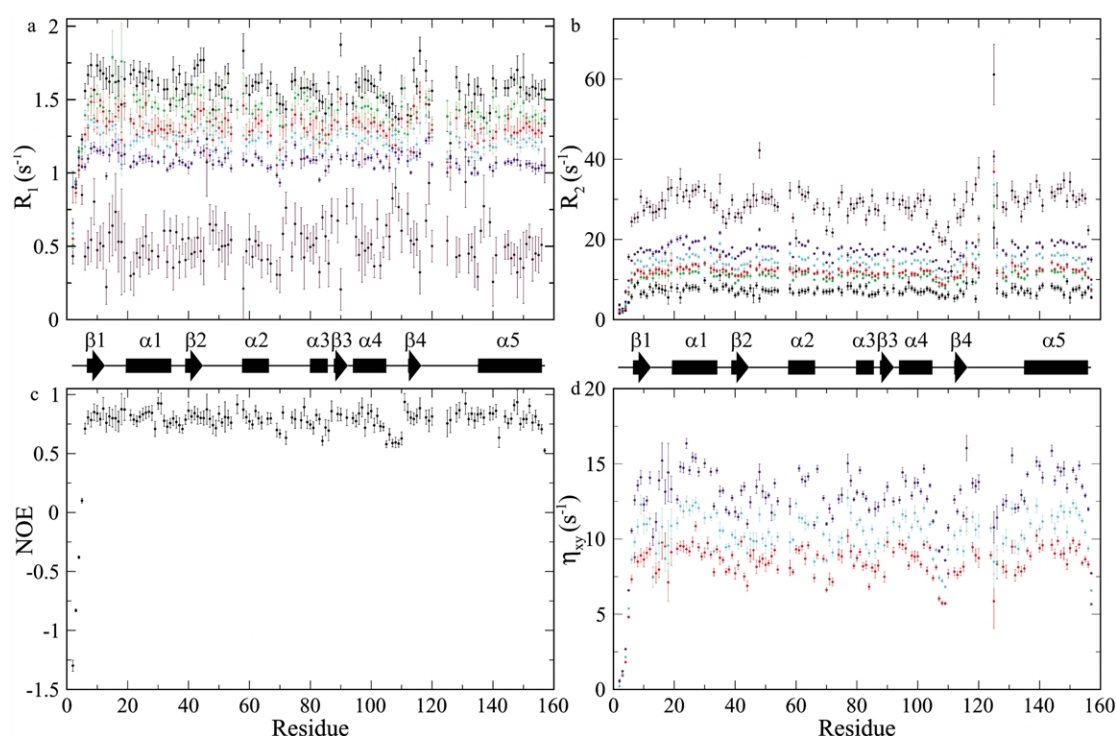


Figure 5. ^{15}N -relaxation parameters obtained for LMW-PTP at concentrations of 0.167 mM (green; (a) and (b) only), 0.34 mM (red), 0.66 mM (cyan) and 1.24 mM (blue), and extrapolation to monomer (black) and dimer (brown). The color coding is the same as in Figure 1. (a) R_1 relaxation rates. The average values at the four different concentrations, in the order listed above, are: $\langle R_1 \rangle = 1.40(\pm 0.07) \text{ s}^{-1}$; $1.30(\pm 0.08) \text{ s}^{-1}$; $1.22(\pm 0.05) \text{ s}^{-1}$; and $1.07(\pm 0.05) \text{ s}^{-1}$. (b) R_2 relaxation rates. The average values (as in Figure 1(a)) are: $\langle R_2 \rangle = 10.85(\pm 1.09) \text{ s}^{-1}$; $11.81(\pm 1.22) \text{ s}^{-1}$; $14.15(\pm 1.53) \text{ s}^{-1}$; and $17.12(\pm 1.83) \text{ s}^{-1}$. (c) ^{15}N -NOEs reported as the average value from the three highest concentrations. (d) η_{xy} relaxation rates at each of the three highest concentrations. The average values at the different concentrations, in the order listed above, are: $\langle \eta_{xy} \rangle = 8.20(\pm 1.23) \text{ s}^{-1}$; $9.71(\pm 1.68) \text{ s}^{-1}$; and $11.89(\pm 2.05) \text{ s}^{-1}$. In calculating the averages for (a), (b) and (d), residues 2–6 and 157 were not included. The secondary structure elements are indicated at the top. The graphs were made using Grace (Grace Development Team).

ranging from $0.026(\pm 0.002)$ to $1.24(\pm 0.07) \text{ mM}$. Non-linear least-squares optimization³¹ was used to fit the monomer–dimer model (equation (4)), simultaneously against multiple data pairs of chemical shifts and protein concentrations. The largest ^1H chemical shift changes (observed for the backbone H^{N} of residues Ser47, Asp48, Trp49, Asn50, Asp129, and the side-chain H^{e} of Trp49, see Figure 2), resulted in a dissociation constant of $K_{\text{d}} = 1.5(\pm 0.1) \text{ mM}$. The corresponding result for ^{15}N chemical shifts (residues Ser47, D48, Trp49, Asn50, Ile127, Tyr131, Tyr132, Gly133, and Trp49 N^{e}) is $K_{\text{d}} = 1.6(\pm 0.2) \text{ mM}$, in agreement with the results from the ^1H data. The higher precision of the ^1H data set is due to larger shift changes relative to linewidths, and higher digital resolution in the ^1H dimension of the spectra. The NMR results agree well with the dissociation constant estimated previously by analytical ultracentrifugation analysis.¹⁸ Relative populations of monomer and dimer at the different concentrations were calculated using the more precise value of K_{d} determined from the ^1H -shift data.

We estimated K_{d} at two additional temperatures, 17°C and 27°C (data not shown). At 27°C , $K_{\text{d}} = 0.5(\pm 0.2) \text{ mM}$. At 17°C , the analysis was

limited by serious line broadening of the NMR spectrum, which is caused in part by increased transverse relaxation rates (slower rotational diffusion) at the lower temperature, and in part by increased population of dimers at a given sample concentration. However, it is clear that K_{d} decreases monotonically, and we can estimate that the value falls approximately in the range 0.1 – 0.3 mM at 17°C . Hence, dimerization is associated with a favorable (negative) change in enthalpy, as observed from a van't Hoff plot of $-\ln K_{\text{d}}$ versus $1/T$.

Extraction of relaxation data for the monomeric and dimeric states

^{15}N relaxation measurements were performed on four samples with concentrations of 0.17, 0.34, 0.66, and 1.24 mM, corresponding to monomer populations of $0.85(\pm 0.01)$, $0.76(\pm 0.01)$, $0.65(\pm 0.01)$, and $0.54(\pm 0.02)$, respectively. R_1 and R_2 experiments were performed on all four samples (Figure 5(a) and (b)), while the inherently less sensitive $\{^1\text{H}\}$ - ^{15}N NOE and η_{xy} experiments were performed on the three most concentrated samples only (Figure 5(c) and (d)). The R_1 and R_2 relaxation

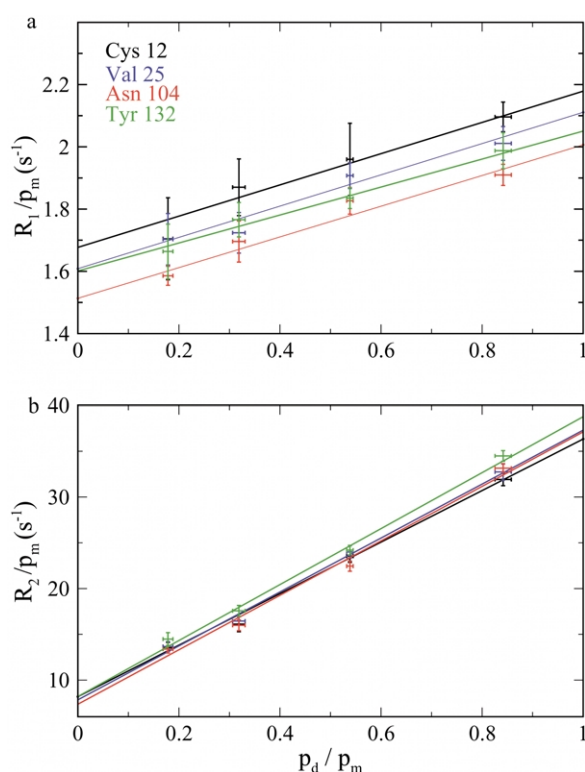


Figure 6. Extraction of relaxation rates for the monomeric and dimeric states by fitting equation (6) to the experimental data. (a) R_1 rates. (b) R_2 rates. Representative examples are shown for four different residues: Cys12 (black); Val25 (blue); Asn104 (red); Tyr132 (green). The graphs were made using Grace (Grace Development Team).

rate constants were significantly concentration-dependent, thus making possible the analysis according to equation (6), as exemplified in Figure 6. The extrapolated rate constants for the monomeric and dimeric states are included in Figure 5(a) and (b). The average relaxation rates for the monomer and dimer, excluding residues 2–6 and 157, are $\langle R_1 \rangle = 1.57 (\pm 0.10) \text{ s}^{-1}$ and $0.50 (\pm 0.13) \text{ s}^{-1}$, respectively, and $\langle R_2 \rangle = 7.24 (\pm 0.99) \text{ s}^{-1}$ and $27.4 (\pm 3.9) \text{ s}^{-1}$, respectively. Since the monomer is more heavily populated over the concentration range covered here, the data extracted for the monomer are of superior quality compared to those for the dimer, which are sensitive to extrapolation errors. Large relative errors result from the extrapolation to R_1 values for the dimer, thereby limiting the analysis and interpretation of the relaxation data in terms of motional parameters for this state. The R_1 and R_2 relaxation rates observed here for LMW-PTP are strongly concentration-dependent. Detailed spin relaxation studies of proteins in monomer–dimer equilibrium have been presented previously,^{30,32–34} but those studies did not attempt to extract separate relaxation rates for the monomeric and dimeric states. In the present case, the large difference in rotational diffusion properties between the monomer and dimer (see below), and the presence of a

structural model for the dimer make the separation of relaxation rates tractable. However, as mentioned above and described further below, the relaxation rates extracted for the dimer are compromised by extrapolation errors and possible existence of non-negligible populations of higher-order oligomers at higher concentrations, which limits the reliability of the results for the dimer.

The NOE data were not sufficiently concentration-dependent to enable extraction of data for the monomeric and dimeric states according to equation (6). This may be expected because the heteronuclear NOE is relatively insensitive to the order parameter, and depends only weakly on the correlation time for overall rotational diffusion. The absence of any significant concentration dependence of the NOE does indicate that there are no large differences between the monomeric and dimeric states in their backbone dynamics on a time scale of hundreds of picoseconds. The NOE values obtained at the different concentrations were co-added to yield a single value for each residue (Figure 5(c)) that was used in the following model-free analysis.

The η_{xy} data exhibit a clear concentration dependence (Figure 5(d)). However, the lack of data at the lower concentration severely biases the linear extrapolation, yielding η_{xy} rates that are unreasonably low for the monomer, and *vice versa*. Therefore, we used the η_{xy} data only to estimate the exchange contributions to R_2 at each of the three concentrations (see equation (7)). This approach serves two purposes. First, it enables identification of those residues that exhibit significant exchange, which is an important step in the model-free analysis of fast time scale dynamics and rotational diffusion. Second, in certain cases the concentration-dependent data enable a qualitative assessment of whether the observed exchange is primarily due to monomer–dimer exchange or intramolecular exchange, as well as an indication of any changes in the exchange dynamics that result from dimerization.

Microsecond to millisecond timescale dynamics

The ¹⁵N chemical shift is sensitive to the backbone torsion angles,³⁵ hydrogen bonding distance³⁶ and electrostatic fields from nearby charges.³⁷ Hence, time-dependent modulation of these parameters due to conformational dynamics on μ s–ms time scales may yield significant exchange contributions, R_{ex} , to the transverse relaxation rates. Contributions from monomer–dimer exchange to the R_2 rates can occur only for those residues that differ in ¹⁵N chemical shift between the monomer and dimer, i.e. those that exhibit concentration-dependent chemical shift changes (see Figures 2 and 3). In the case of pure monomer–dimer exchange, the R_{ex} terms should increase with concentration over the entire range covered here (see equation (8)). Chemical shift changes

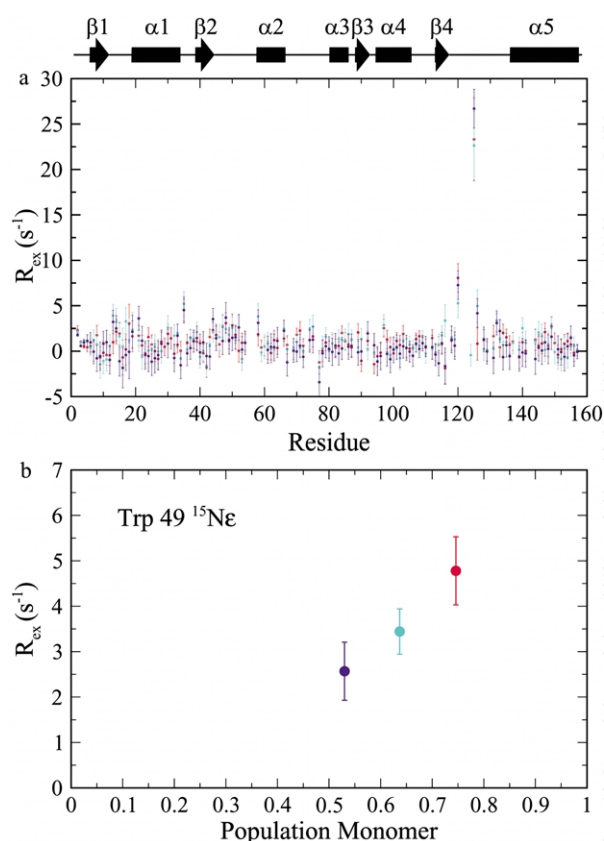


Figure 7. Exchange terms, R_{ex} , evaluated according to equation (7) at each of the three highest concentrations, 0.34 mM (red), 0.66 mM (cyan) and 1.24 mM (blue). (a) R_{ex} plotted versus amino acid sequence number. (b) R_{ex} plotted versus monomer population for the side-chain ^{15}N of Trp49. The graphs were made using Grace (Grace Development Team).

also result if dimerization affects the relative populations of two conformations involved in intramolecular exchange. If the relative populations become more skewed upon dimerization, or if only a single conformer exists in the dimer, then the R_{ex} terms may decrease with increasing concentration.

Exchange contributions to the transverse relaxation rates of the backbone amide nitrogen atoms were estimated according to equation (7) at each of the three highest concentrations (0.34, 0.66 and 1.24 mM). Figure 7(a) shows the resulting values of R_{ex} at each concentration, as a function of residue number. Elevated levels of R_{ex} are noticeable for stretches of residues in the P-, W-, and D-loops, all of which are directly involved in the function of the enzyme. All residues that show significant ^{15}N chemical shift changes upon dimerization also show signs of exchange, although the values of R_{ex} are generally small. In addition, several residues that do not exhibit concentration-dependent chemical shift changes also have sizeable R_{ex} terms. For most residues, the concentration dependence of R_{ex} is small compared to the uncertainties (Figure 7(a)). Figure 7(b) shows R_{ex} plotted

against monomer population for the indole ^{15}N of Trp49, which displays significant concentration dependence of both the chemical shift and R_{ex} . As can be seen, the Trp49 side-chain exhibits a clear tendency of decreasing R_{ex} with increasing protein concentration. This behavior is opposite to that expected for pure monomer–dimer exchange, but can be explained by a reduction of intramolecular exchange upon dimerization. The same tendency is observed also for Ser47 and Asn50, although the R_{ex} terms and the concentration dependence of these are much smaller than what is observed for the Trp49 side-chain. Apparently, the Trp49 side-chain, and possibly also the backbone, experiences μs – ms time scale dynamics in the monomer that are reduced or quenched upon dimer formation. This can be explained based on the monomer and dimer structures. The Trp49 side-chain, which is located at the outer rim of the active site, is solvent-exposed in the monomer,^{16,38} but is buried in the interaction surface of the dimer.¹⁸ The side-chain orientation differs by $\sim 90^\circ$ between the monomer and dimer crystal structures. Together, these results suggest that the side-chain undergoes exchange between (at least) two different conformations in the monomer, and that dimer formation selects one of these pre-existing conformations. Interestingly, Trp49, Asn50 and Arg53 were previously shown to be important for specificity in target binding.²⁴ The present results, together with the available structural data, offer additional insights into the molecular basis for the observed selectivity in target binding.

In the P-loop, Gly14 exhibits minor, but significant exchange, $R_{\text{ex}} \approx 3 \text{ s}^{-1}$. The surrounding residues Leu13 and Asn15 also show minor R_{ex} terms, together with Cys17, Arg18, Ala19 and Ile21. In all cases, the exchange rate is small, $R_{\text{ex}} \leq 4 \text{ s}^{-1}$. Notably, all backbone amides of residues 13–18 are hydrogen bonded to the phosphate in the crystal structure,¹⁶ while Ile21 is hydrogen bonded to the carbonyl group of Arg18. The minor exchange observed in the P-loop could be an effect of the monomer–dimer equilibrium, or could perhaps be explained by small-scale fluctuations of the hydrogen bonding distances³⁶ and backbone position relative to the phosphate ion, because the effects of electrostatic fields on the ^{15}N chemical shift can be sizeable.³⁷ Significant and concentration-independent exchange is also observed for Ile35, which forms a hairpin hydrogen bond in a loop segment between $\alpha 1$ and $\beta 2$ on the opposite side of the molecule from the active site. This region also has increased atomic displacement factors (B -factors) in both the monomer and dimer crystal structures.

In the D-loop, the entire stretch of residues from 120 to 127 are involved in μs – ms conformational exchange. Residues Asp120, Leu125 and Ile126 have large R_{ex} terms that are not significantly concentration-dependent. None of these three residues are located in the dimer interaction surface, and they do not show significant ^{15}N chemical shift

changes upon dimer formation, indicating that R_{ex} in these cases reflects intramolecular dynamics that are present in both the monomer and dimer. In addition, Gln124 and Ile127 are too exchange broadened to permit detailed analysis of the relaxation rates, and Gln122 and Lys123 are not observable in the spectrum, presumably due to extensive exchange broadening. No data are available for residue 121, because this is a proline. The segment 120–123 forms a type I β -turn, with Lys123 in a left-handed α -helical conformation. Following the turn, the segment 124–126 is kinked, with the backbone torsion angles of Gln124 and Ile126 in β -strand conformation, but Leu125 in α -helical conformation. Residues 127–129 all have an extended backbone conformation. Ile127 is the only residue in the D-loop that is hydrogen bonded to a different secondary structure element (Ile127 HN to Met91 O). The broadening of the Ile127 cross-peak suggests that the Ile127 HN–Met91 O hydrogen bond is broken transiently during the conformational exchange of the D-loop. In contrast, the backbone amides of Glu128 and Asp129 are not hydrogen bonded in the crystal structure, and they are not located at the dimer interaction surface. Note also that neither of these two residues show significantly concentration-dependent ^{15}N chemical shifts. It may not be surprising that these two residues do not show any signs of conformational exchange, because motions of the D-loop may not modulate the local backbone environment of these residues. From a structural point of view, it appears very likely that the dihedral angles and hydrogen bonds of the segment 120–127 undergo significant rearrangements when the D-loop exchanges between the different conformations that have been proposed for the engagement of Asp129 during the catalytic cycle. It is conceivable that the conformational change has the character of a hinged loop movement, as observed previously for the larger PTPs.^{7–9} Based on the present results we speculate that the hinge regions may correspond to the two β -turns (120–123 and 130–133) at each end of the D-loop. The present results suggest that the D-loop undergoes conformational fluctuations relative to other parts of the protein. Importantly, the exchange process of the D-loop is present in both the monomer and dimer, and appears to be unaffected by dimerization and, by inference, target binding. Similar observations of active-site loop dynamics that prevail in the ligand (inhibitor)-bound state have been made for ribonuclease binase.³⁷ Assuming a maximal chemical shift difference of 10 ppm and two-state exchange (cf. equation (8)), the values of R_{ex} observed for Asp120, Leu125 and Ile126, together with the broadening beyond detection of certain residues in the D-loop, enable us to estimate that the microscopic exchange rate falls in the range $k_{\text{ex}} \sim 10^2$ – 10^4 s^{-1} . The catalytic rate constant of LMW-PTP is $k_{\text{cat}} \approx 30 \text{ s}^{-1}$.^{10,14} k_{cat} is limited by dephosphorylation of the covalent phosphoenzyme intermediate (step 3 of Scheme 1), which occurs with a rate of

$k_3 \approx 35 \text{ s}^{-1}$, while the phosphorylation of Cys12 (step 2) is a considerably faster step with $k_2 \approx 540 \text{ s}^{-1}$,¹⁴ as measured for the activated substrate pNPP; with natural substrates k_2 is expected to be significantly smaller. As noted above, Asp129 is required for step 2 of the reaction.^{25,39} Because k_{ex} is the sum of the forward and backward rate constants, it is quite possible that one of these rates is similar to k_2 . Thus, the dynamics of the D-loop occur with an exchange rate that compares rather well with the rate constant of the relevant reaction step, suggesting that the intramolecular dynamics could be coupled to enzyme catalysis in this system. However, further investigations are needed to establish the correspondence between these rates, and to verify that the dynamics observed in the D-loop does involve Asp129.

Residues Pro130–Gly133 form a type I β -turn that connects the D-loop with $\alpha 5$. In the monomer the β -turn is solvent-exposed, whereas Tyr131, Tyr132 and Gly133 are packed against the other molecule in the dimer structure, and they all show significant concentration-dependent chemical shift changes in the ^{15}N -dimension. Hence, these residues are likely to be affected by line broadening due to monomer–dimer exchange. Tyr132 shows significant exchange ($R_{\text{ex}} \approx 3.5 \text{ s}^{-1}$) that is concentration-independent, suggesting that also the intramolecular dynamics of the D-loop may affect the chemical shift of this residue. In contrast, Gly133 provides an example of a residue experiencing increasing R_{ex} with increasing concentration, although the effect is small ($R_{\text{ex}} = 0.4(\pm 1.1)$, $1.3(\pm 1.1)$, and $2.2(\pm 1.3) \text{ s}^{-1}$ for 0.34, 0.66, and 1.24 mM concentrations, respectively). The estimated chemical shift difference between monomeric and dimeric states is $\Delta\delta = 0.93(\pm 0.06) \text{ ppm}$. Assuming that Gly133 experiences only monomer–dimer exchange, we can estimate the rate of dimer dissociation to be on the order of $k_{\text{off}} \sim 10^4 \text{ s}^{-1}$, which agrees with the dissociation constant ($K_{\text{d}} = 1.5 \text{ mM}$) and the expected on-rate for protein dimerization reactions ($k_{\text{on}} \sim 10^6$ – $10^7 \text{ M}^{-1}\text{s}^{-1}$).⁴⁰ While this value of k_{off} is a very rough estimate, it is in general agreement with the modest R_{ex} values observed for those residues that show concentration-dependent chemical shifts. It should be noted that the large majority of concentration-dependent chemical shifts used to determine the dissociation constant extrapolate to shift differences between monomer and dimer that are approximately one order of magnitude smaller than the microscopic exchange rate, indicating that the assumption of fast exchange is fulfilled, so that equation (3) is valid.

Overall rotational diffusion

The R_2 and R_1 rates extracted for the monomer and dimer (Figure 5(a) and (b)) directly reveal that there is a larger dispersion in the values for the dimer than the monomer, indicating that rotational

diffusion is significantly more anisotropic for the dimer, as expected based on the available structures. For the monomer, both the isotropic and anisotropic models of rotational tumbling satisfy the experimental data, but the improvement in the fit achieved with the more complex model is not statistically significant, as determined by an F -test ($p = 0.28$).⁴¹ Based on the ratios of the principal components of the inertia tensor (1:0.82:0.72), monomeric LMW-PTP is expected to have slightly anisotropic rotational diffusion. However, the relatively large uncertainties in the relaxation rates extracted for the monomer reduce the possibility to discriminate between different models. Because the uncertainties are larger than normal (e.g. compare with those estimated at each individual concentration, Figure 5(a) and (b)), the reduced χ^2 -statistic (1.07) is significantly lower than typically observed in previous studies.⁴² The isotropic rotational correlation time is $\tau_{c,m} = 5.92(\pm 0.05)$ ns, which is in good agreement with the value expected from Stokes' law (5.6 ns), calculated using the viscosity of water at 37 °C, $\eta_w = 0.665$ Ns/m², and a hydration shell of 3.2 Å.⁴³ We also performed hydrodynamic model calculations using the program HYDRONMR,⁴⁴ which yielded a value of 7.0 ns. Published data on τ_c for proteins of nearly the same size as LMW-PTP reveal slightly larger values when scaled to 37 °C. Seven proteins included in the data base compiled by Krishnan & Cosman⁴⁵ have molecular weights within ± 1 kDa from that of LMW-PTP ($M_r = 17.91$ kDa); the average and standard deviation is $17.59(\pm 0.56)$ kDa. For this set of proteins, τ_c ranges between 5.92 and 8.45 ns, with an average and standard deviation of $7.22(\pm 1.02)$ ns. The protein of most similar size ($M_r = 17.97$; cyclophilin A⁴⁶) has $\tau_c = 6.24$ ns, which is similar to the experimental value for monomeric LMW-PTP. Reassuringly, the reasonable agreement between the experimental and theoretical results indicates that extraction of relaxation data by extrapolation is viable for the monomer. The isotropic model was used in the ensuing model-free analysis. In contrast to the data extracted for the monomeric state, the isotropic model did not satisfy the raw experimental relaxation data obtained at any of the four protein concentrations.

In the case of the dimer, the extracted ratios R_2/R_1 have very large uncertainties, and both the isotropic and anisotropic models fit the data, but the anisotropic model is significantly better than the isotropic model, with $p = 0.0012$. The principal components of the anisotropic diffusion tensor for the dimer are $D_{xx} = (6.0 \pm 0.1) \times 10^6$ s, $D_{yy} = (7.0 \pm 0.1) \times 10^6$ s, and $D_{zz} = (8.4 \pm 0.1) \times 10^6$ s, giving an average rotational correlation time of $\tau_{c,d} = 23.4(\pm 0.6)$ ns. The LMW-PTP dimer has a nearly prolate shape (Figure 3), and the inertia tensor is substantially anisotropic with principal component ratios of 1:0.91:0.29. The orientations of the diffusion and inertia tensor principal axes nearly coincide; the

angles between them are 4°, 18° and 18° for the x , y , and z -axis, respectively. Perrin's equations for a prolate ellipsoid⁴⁷ with an axial ratio of $((1 + 0.91)/(2 \times 0.29))^{1/2} = 1.8$ and stick boundary conditions yield an average rotational correlation time of 12.6 ns, which is only 54% of the experimental value. Also, the Perrin equations predict the ratio of the diffusion constants around the two axes to be $D_r = 1.67$, which should be compared with the experimental value of $D_r = 1.29$. HYDRONMR⁴⁴ calculations predict a rotational correlation time of 17.1 ns and $D_r = 1.80$. The discrepancies between the experimental and theoretical results for the dimer suggest that a non-negligible population of higher-order oligomer, e.g. tetramer (which is expected to be less anisotropic than the dimer), is present at higher protein concentrations. However, concentration-dependent chemical shift perturbations are observed only for residues located in, or close to, the dimer interface, as discussed above. Furthermore, various models that include tetramers (viz. monomer–dimer–tetramer and monomer–tetramer equilibria) do not improve the fit to the concentration-dependent chemical shifts over that of the monomer–dimer model. Hence, the self-association appears to be dominated by a monomer–dimer equilibrium over the range of concentrations covered here. Given the available data, we conclude that the self-association of LMW-PTP, as monitored by the concentration dependence of the chemical shifts, is adequately described by the monomer–dimer model. The presence of non-specific higher-order oligomers at the higher concentrations will primarily bias the results extracted for the dimer, whereas the monomer data will be less affected.

Model-free analysis of the monomer

Model-free analysis of the monomer equilibrium fluctuations was performed using the relaxation rate constants extracted from the four data sets obtained at different concentrations. Five different motional models were used in the model-free analysis, as described in Material and Methods. The number of residues optimized with models 1–5 were: 106, 13, 5, 1, and 4, respectively. In the present work the monomer relaxation rates were obtained by extrapolation. Therefore, it is particularly important to compare the resulting order parameters against previously reported data and structural features of the protein, so as to assess the credibility of the obtained results. Figure 8 shows the order parameters plotted *versus* residue number, and Figure 9 shows the order parameters encoded on the structure. The gross features of the amplitudes of fluctuations reported by the order parameters compare well with the atomic displacement factors (B -factors) from the crystal structure (1PNT;¹⁶ data not shown). In addition, order parameters of individual residues generally can be explained in terms of local structure, as outlined further below. At the N terminus, residues 2–4

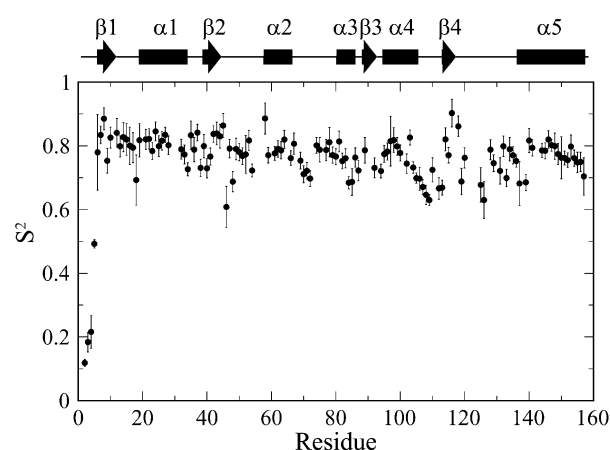


Figure 8. Order parameters, S^2 , of monomeric LMW-PTP plotted *versus* residue number. The secondary structure elements are indicated at the top. The graph was made using Grace (Grace Development Team).

have very low order parameters of $S^2 \leq 0.2$, indicating nearly unrestricted motion. Thr5 also exhibits a large amplitude of motion with $S^2 = 0.49$. All residues in $\beta 1$ (6–12) are relatively rigid with a weighted mean order parameter of $\langle S^2 \rangle = 0.83(\pm 0.04)$. In the P-loop (12–19), all residues have high order parameters, with $\langle S^2 \rangle = 0.80(\pm 0.03)$, except for the catalytically important Arg18 ($S^2 = 0.69$), which is also the first residue of $\alpha 1$. Clearly, the P-loop is rigid on the sub-nanosecond time scale in the phosphate-bound solution state, as expected from the dense network of hydrogen bonds between the phosphate oxygen

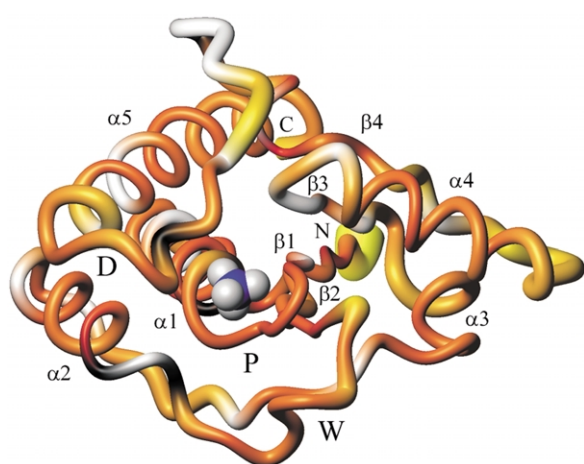


Figure 9. Order parameters, S^2 , color-coded on the crystal structure of monomeric LMW-PTP (1PNT¹⁶). The locations of the P-, D-, and W-loops are indicated (D, P, W). The secondary structure elements are labeled $\alpha 1$ – $\alpha 5$ and $\beta 1$ – $\beta 4$. S^2 is encoded using both color and the backbone tube radius, ranging continuously from yellow to red and 0.3–2.6 Å, respectively, for S^2 ranging from 0 to 1. White indicates residues that were not included in the analysis and black indicates proline residues; for these residues, the backbone radius was calculated as the average value from the bracketing residues. The bound phosphate ion is shown as space filling model. The picture was prepared using Molmol.⁶⁹

atoms and the backbone amide nitrogen atoms.¹⁶ Of note, the rigidity of the P-loop is probably required to promote the observed enhancement of hydrogen bonds in the transition state.¹⁷ The high order parameters are also in agreement with the low B -factors observed for these residues in the crystal structure. Except for Arg18, the entire $\alpha 1$ helix (residues 18–32) following the P-loop is rigid, $\langle S^2 \rangle = 0.81(\pm 0.03)$. Residues Asn34 and Asn38 in the loop connecting $\alpha 1$ with $\beta 2$ show some flexibility ($S^2 \approx 0.73$), while the rest of the loop is more constrained, $\langle S^2 \rangle = 0.77(\pm 0.05)$. In $\beta 2$ (residues 39–45), Val40 and Ile41 have $S^2 \approx 0.73$, while the others all have high order parameters between 0.80 and 0.86, yielding $\langle S^2 \rangle = 0.80(\pm 0.05)$ for the entire strand. The lower order observed for Val40 and Ile41 may be explained by the fact that Val40 is hydrogen bonded to the first residue in $\beta 1$, and Ile41 HN is the only backbone amide group in the strand that is not hydrogen bonded. In the W-loop (residues 46–56), Val46, Asp48, and Ser54 show significantly lower order parameters ($S^2 = 0.61$, 0.69, and 0.72, respectively) than the rest of the loop residues, which have values in the range $S^2 = 0.77$ –0.82. These differences in S^2 appear to reflect differences in the hydrogen bonding patterns of the loop residues. The amides of Asp48 and Ser54 are not hydrogen bonded in the crystal structure, whereas Val46 is involved in a bifurcated hydrogen bond. Possibly, the low order parameter of Val46 may be due to sub-nanosecond reorientations between different hydrogen bonding patterns that cause large-amplitude rotational fluctuations of the N–H bond vector. The only other non-hydrogen bonded amide in the W-loop is Asn50 ($S^2 = 0.78$), which is located in a tight β -turn involving residues 48–51. The Pro-Asp-Pro motif of residues 55–57 leaves an information gap, because Asp56 is excluded from the analysis due to spectral overlap. The backbone amides of $\alpha 2$ (residues 58–66) have $\langle S^2 \rangle = 0.79(\pm 0.03)$, including Arg58, which is very rigid with $S^2 = 0.89$. In the long loop (residues 67–79) connecting $\alpha 2$ and $\alpha 3$, residues 67–72 show a decreasing trend in order parameters (from $S^2 = 0.81$ for Gly67) towards the middle of the loop ($S^2 = 0.70$ for His72). This trend is interrupted at Ala74, which has $S^2 = 0.80$. The pattern of S^2 can be explained by the hydrogen bonding pattern for this stretch of residues: the amide and carbonyl groups of Ala74 are hydrogen bonded to Gly52 and Arg53 in the W-loop; in contrast, none of residues 68–73 are involved in backbone hydrogen bonds. The short and irregular 3_{10} helix $\alpha 3$ (residues 80–84) is relatively flexible, $\langle S^2 \rangle = 0.74(\pm 0.05)$, except for Asp81 ($S^2 = 0.81$), which is hydrogen bonded to Thr78. Val83 has the second largest order parameter ($S^2 = 0.76$), and is hydrogen bonded to Glu80. Order parameters are available only for Tyr87 and Leu89 ($S^2 = 0.72$ and 0.79, respectively) in the short strand $\beta 3$ (residues 87–90). Helix $\alpha 4$ (residues 92–104) have $\langle S^2 \rangle = 0.77(\pm 0.04)$, with higher values ($S^2 \approx 0.82$) in the middle of the helix, as characteristically

observed.⁴⁸ The loop following $\alpha 4$ (residues 105–111) and the first two residues of $\beta 4$ (112 and 113) is the longest stretch of consecutive amino acid residues that exhibit low order parameters ($\langle S^2 \rangle = 0.67(\pm 0.03)$), indicating a large degree of flexibility for this region. These residues also have large B -factors in the crystal structure. Residues 104–110 all have significant values of τ_e ranging from 18 to 46 ps, indicating that the relatively large amplitude fluctuations of these residues have appreciable correlation times. Glu114 and Leu115 in $\beta 4$, and Leu116 and Ser118 in the following segment with irregular secondary structure, all exhibit high order parameters between $S^2 = 0.77$ – 0.90 , again in good agreement with the crystallographic B -factors. In the long and extended segment from 119 to 129, order parameters were obtained only for 119–120, 125–126 and 128–129. Asp120 is located in a β -turn involving 120–123, and has $S^2 = 0.76$. Residues 119, 125–126 are flexible with S^2 in the range 0.63–0.69. The relatively large degree of disorder for this segment is also reflected by the B -factors. Clearly, the region 120–127 exhibits extensive conformational fluctuations on both ps–ns and μ s–ms timescales, as discussed further above. Glu128 and the catalytically essential Asp129 both have somewhat higher values of S^2 (0.79 and 0.75, respectively), compared to the other residues in the extended part (124–129) of the D-loop. Residues 130–133 form a β -turn, with values of S^2 in the range 0.70–0.80, that connects the C-terminal end of the D-loop to the long helix $\alpha 5$ (residues 135–157). The mean order parameter in $\alpha 5$ is $\langle S^2 \rangle = 0.77(\pm 0.03)$. Again, the middle of the helix is characterized by higher values of S^2 (0.80–0.82) than the termini.

Excluding residues 2–6 and 157, the global mean order parameter is $\langle S^2 \rangle = 0.76(\pm 0.05)$, which is significantly lower than the average value of 0.858 calculated from a database of order parameters in 20 proteins,⁴⁸ but similar to the average order parameter in dihydrofolate reductase (0.79 ± 0.09)⁴⁹ and glucose permease IIA domain (0.76 ± 0.14).⁵⁰ The low average order parameter of LMW-PTP may be related to the fact that its structure contains several long and extended loop-like segments that are sparsely hydrogen bonded to the rest of the protein (see Figure 1). A potential caveat is that the presence of higher-order oligomers at the higher protein concentrations will result in τ_c being underestimated, which in turn will yield systematically underestimated order parameters. All together, the order parameters calculated for the monomeric state of LMW-PTP are consistent with what can be expected based on the structural features, as well as with the crystallographic B -factors. This serves as a validation of the approach employed here to extract order parameters and dynamical information from a series of relaxation rate measurements at different protein concentrations, and shows that meaningful results can be obtained even though the analysis is complicated by protein oligomerization.

Model-free analysis of the dimer

The model-free parameters obtained for the dimer generally have large uncertainties, and several residues in the dimer have inordinate S^2 values that are either close or equal to 1, or much reduced from the value obtained for the monomer (results not shown). These aberrant values could possibly be explained by deviations of the equilibrium N–H bond vector orientations between the solution and crystal states, or deviations between the actual and optimized orientation of the diffusion tensor in the molecular frame. However, as outlined above, the discrepancies may also arise because of extrapolation errors and/or the possible existence of higher-order oligomers at higher concentrations. Excluding these outlying data, the global mean order parameter for the dimer is $\langle S^2 \rangle = 0.85(\pm 0.07)$, which is higher than the monomer value, but in agreement with the average value of the database mentioned above.⁴⁸ In nearly all cases where significant differences are observed, the order parameters are higher in the dimer than in the monomer. There is the possibility that S^2 is systematically inflated if the global rotational correlation time has been overestimated.⁵¹ Considering these caveats, a detailed comparison of S^2 between the two states is not meaningful. Nonetheless, certain general features may be discerned in the difference in order parameter observed for segments of residues. Notably, the central β -sheet comprising strands $\beta 1$ – 2 is largely unaffected by dimerization. The same is true for the central part of $\alpha 1$, which packs against the β -sheet, and for the N-terminal part of $\alpha 5$, which packs against $\alpha 1$. Hence, it appears that LMW-PTP has a stable core with order parameters that compare well with those typically observed in secondary structure elements. The fast time scale fluctuations of this core do not appear to be affected by oligomerization. In contrast, increased order is observed for the majority of loop residues, including those that form the dimer interface, together with connecting parts of secondary structure elements. Considering only pair-wise differences between the monomer and apparent dimer that are significant at the 98% level (i.e. differences that are larger than two times the standard deviation in the difference), it is clear that the W-loop is significantly more rigid in the dimer. The long loop (residues 67–79) that connects $\alpha 2$ and $\alpha 3$ is affected only in the region (72–75) that packs against the W-loop.

Material and Methods

Sample preparation and determination of protein concentration

Uniformly ^{15}N -labeled bovine heart LMW-PTP was expressed in *Escherichia coli* BL21(DE3) cells harboring the pET-11d vector that contained the gene, using ^{15}N -enriched M9 minimal medium. The protein was purified

essentially following procedures described.⁵² An initial purification step using SP-Sepharose ion-exchange chromatography yielded fractions that were 90–95% pure. After pooling and concentration of the fractions, a single step of gel filtration on Sephadex G50 columns yielded the pure protein. The enzyme activity was followed during expression and purification using a simple assay, as follows: 5–50 μ l of crude sample was mixed with 3 ml of 0.3 mg/ml *p*-nitrophenylphosphate (pNPP) dissolved in 133 mM Tris-HCl (pH 8.0); the reaction mixture was incubated at room temperature for 20 minutes, after which the reaction was quenched by adding 0.5 ml 3 M NaOH; the amount of product formed was evaluated by measuring the absorbance at 405 nm.

LMW-PTP samples of concentrations ranging from 0.026 to 5 mM were prepared in argon or helium purged buffer containing 200 mM K_2HPO_4/KH_2PO_4 , 10 mM DTT, 3 mM NaN_3 , and 10% 2H_2O , at pH 5.0. The pH was adjusted by adding small amounts of 1 M K_2HPO_4 to a stock solution of 1 M KH_2PO_4 . The protein concentration was determined by UV absorbance at 280 nm. In order to maximize sensitivity and minimize the effect of possible differences in absorbance at different concentrations the samples were diluted to $A_{280} \approx 1.0$ prior to measurement. All pipettes used were calibrated gravimetrically, and the standard errors in the volume measurements were estimated by calculating the standard deviation of eight or nine replicates at each volume. One standard deviation corresponded to 0.2–3.9%, with the highest precision obtained for the largest volume. Standard errors of the UV absorption measurements were estimated from five replicates. The concentrations in absorbance units were determined to be: $0.564(\pm 0.008)$, $1.69(\pm 0.03)$, $3.59(\pm 0.03)$, $7.18(\pm 0.06)$, $14.2(\pm 0.3)$ and $26.5(\pm 0.3)$ AU (A_{280}). These values were converted to molar concentrations using the relationship $1 \text{ AU } (A_{280}) = 0.84(\pm 0.05) \text{ g/l}$, as determined from protein hydrolysis followed by amino acid HPLC analysis of a single sample. The standard error of each concentration measurement was estimated by error propagation. The molar protein concentrations were determined to be: $0.026(\pm 0.002)$, $0.079(\pm 0.005)$, $0.17(\pm 0.02)$, $0.34(\pm 0.03)$, $0.66(\pm 0.04)$, and $1.24(\pm 0.07)$ mM; the relative uncertainty in molar concentration is 6%. All data manipulation and calculations were carried out using concentrations in absorbance units, and the final result (K_d) was subsequently converted to molar quantities.

Nuclear magnetic resonance spectroscopy

All NMR experiments were performed at $37.0(\pm 0.1)^\circ\text{C}$, unless otherwise stated, on Varian Inova 600 MHz spectrometers. All spectra were recorded with a spectral width of 8000 Hz sampled over 2048 complex points in ω_2 (1H) and a spectral width of 1865.4 Hz sampled over 128 complex points in ω_1 (^{15}N). As noted previously,¹³ the cross-peaks from the active site loop residues are all severely line broadened at low phosphate concentration, most likely due to conformational exchange on μ s–ms time scales. In a series of 1H – ^{15}N HSQC spectra recorded at 37°C on samples with six different concentrations of potassium phosphate, ranging from 10 to 160 mM, the P-loop cross-peaks increased progressively in intensity up to a concentration of 120 mM, whereafter no further changes were detected (data not shown). To ensure full occupancy of phosphate in the active site, a phosphate concentration of 200 mM

was used here. The initial analysis of LMW-PTP dimerization was based on two-dimensional 1H – ^{15}N heteronuclear single quantum coherence (HSQC)^{53,54} spectra recorded at 14 concentrations ranging from 5 to 0.026 mM. Quantitative determination of K_d involved 1H – ^{15}N HSQC spectra acquired at six protein concentrations ranging from 1.24 to 0.026 mM.

The ^{15}N spin relaxation experiments comprised longitudinal (R_1) and transverse (R_2) relaxation rate constants, and $\{^1H\}$ – ^{15}N steady-state heteronuclear Overhauser enhancement (NOE),^{55,56} as well as transverse 1H – ^{15}N dipolar/ ^{15}N chemical shift anisotropy cross-correlation rate constant (η_{xy})^{57,58} were measured using pulsed-field-gradient sensitivity-enhanced pulse sequences.⁵⁹ The recovery delay between transients was 1.5 seconds and two seconds for the R_1 and R_2 experiments, respectively. The R_1 relaxation delays were (44 (*2), 220, 496, 1057, 1652), (44 (*3), 222, 705 (*2), 1057, 1465, 1916), (44 (*2), 220, 496, 936, 1399, 1916) and (44 (*3), 222 (*2), 705 (*2), 1057, 1465, 1916) ms, and the R_2 delays were (16.0(*2), 48.0, 95.9, 143.9, 207.9), (0.0, 16.0 (*2), 48.0, 64.0 (*2), 95.9, 143.9, 143.9, 207.9), (16.0 (*2), 32.0, 64.0, 96.0, 143.9, 207.9) and (0.0, 16.0 (*2), 48.0, 64.0 (*2), 95.9, 143.9, 143.9, 207.9) ms for the 0.17, 0.34, 0.66 and 1.24 mM samples, respectively. The notations (*2) and (*3) indicate duplicate and triplicate experiments, respectively. The number of transients was 16 for all experiments except for the experiments on the 0.17 mM sample where 40 transients were used. The η_{xy} relaxation delays were (10.9, 21.7, 32.6, 54.3), (10.9, 21.7, 32.6, 43.4, 54.4) and (10.9, 21.7, 32.6, 43.4, 54.3) ms for the 0.34, 0.66 and 1.24 mM samples, respectively; the delays correspond to multiples of $1/J_{NH}$. The number of transients were 48 for the cross-correlation experiment and 16 for the reference experiment for the 0.660 and 1.235 mM samples, and 112 for the cross-correlation experiments and 48 for the reference experiment for the 0.335 mM sample. The $\{^1H\}$ – ^{15}N NOE values were determined as the ratio of the peak intensities from two spectra recorded with and without a four seconds 1H presaturation period incorporated at the end of a six seconds delay between each pulse sequence repetition. The two spectra were recorded in an interleaved manner to ensure identical conditions between the two experiments. The number of transients used were 104, 48 (*2) and 56 for the 0.34, 0.66 and 1.24 mM samples, respectively. Approximate total experiment times were 223 hours for R_1 , 231 hours for R_2 , 235 hours for η_{xy} and 229 hours for the NOE.

Data processing and analysis

NMR spectral processing was performed using NMRPipe.⁶⁰ In order to achieve good resolution over a wide range of linewidths, the dilution titration spectra were apodized using squared sine-bells shifted by 17 degrees and 39 degrees in ω_2 and ω_1 , respectively. The relaxation data were processed using one protocol for optimal sensitivity and one protocol for optimal resolution. In the former spectra were processed using exponential line broadening of 10, 11, 12 and 13 Hz for the 0.17, 0.34, 0.66 and 1.24 mM samples and a cosine-bell in ω_2 and ω_1 , respectively, while the latter spectra were processed using a Lorentzian-to-Gaussian transformation in ω_2 with the same line broadening parameters as indicated above, and a cosine-bell in ω_1 . Linear prediction was used to extend the data size by a factor of two in ω_1 , and both dimensions were zero-filled once. The final size of the frequency domain matrices

was 1900 and 256 real data points in ω_2 and ω_1 , respectively.

NMR data analysis was performed using NMRView.⁶¹ The relaxation data were analyzed using an in-house modified version of the relaxation.tcl NMRView script that directly interfaces with CurveFit (A. G. Palmer, Columbia University). Peak intensities were evaluated as peak heights. Uncertainties of peak heights were estimated from the standard deviation of the base-plane noise. Uncertainties and goodness-of-fit of optimized relaxation parameters were evaluated as described,⁶² using Monte Carlo simulations of the distributions of peak heights.³¹ In some cases, the standard deviations of the peak heights were scaled to give a reduced $\chi^2 = 1$.

Determination of the dimer dissociation constant

The dissociation constant, K_d , of a monomer–dimer equilibrium is defined as:

$$K_d = \frac{[M]^2}{[D]} \quad (1)$$

where $[M]$ and $[D]$ are the concentrations of monomer and dimer, respectively. Alternatively, equation (1) can be written in the form:

$$K_d = \frac{2p_M^2c}{p_D} \quad (2)$$

where p_M and p_D are the populations of protein molecules in monomeric and dimeric states ($p_M + p_D = 1$), respectively, and c is the total protein concentration. For a rate of exchange between the monomeric and dimeric states much faster than the difference in chemical shifts between the two states, the observed resonance frequency, ω_{obs} , is given by the population weighted average of the monomer and the dimer resonance frequencies, ω_M and ω_D :

$$\omega_{obs} = p_M\omega_M + p_D\omega_D = \omega_D + p_M(\omega_M - \omega_D) \quad (3)$$

Combining equations (2) and (3), yields:

$$\omega_{obs} = \omega_D + \frac{\sqrt{K_d(K_d + 8c)} - K_d}{4c}(\omega_M - \omega_D) \quad (4)$$

K_d , ω_M and ω_D were fitted to sets of data pairs consisting of ω_{obs} and c , using non-linear least-squares optimization.³¹ Because the parameters are fitted simultaneously to data for several residues, the dissociation constant can be determined with high precision. A precise and accurate estimate of K_d is of vital importance for separating the monomer and dimer contributions to the measured relaxation rate constants. The dissociation constant, K_d , was determined from a series of HSQC-spectra recorded at the six well-determined concentrations (see Sample preparation). Equation (4) was fitted to the observed chemical shift changes, using Levenberg–Marquardt non-linear least-squares optimization³¹ implemented in Matlab (The MathWorks, Inc.). Uncertainties of the peak positions were assumed to be uniform over the concentration range, and the fit was accepted if the uncertainties gave a reduced $\chi^2 = 1$. In the following step, the chemical shift changes were fitted simultaneously. The uncertainties of the initial fits were multiplied by 1.42 to scale the reduced χ^2 to 1.

Separation of relaxation data for the monomer and dimer

Because exchange due to the monomer–dimer equilibrium is fast relative to the time scale of the spin relaxation, the longitudinal (R_1) and transverse relaxation rates (R_2), and the cross-correlated cross-relaxation (η_{xy}), and the $\{^1H\}$ – ^{15}N heteronuclear nuclear Overhauser effect (NOE), are population weighted averages of these rates in the monomeric and dimeric states.⁶³

$$R_1 = p_MR_{1,M} + p_DR_{1,D} \quad (5a)$$

$$R_2 = p_MR_{2,M} + p_DR_{2,D} + R_{ex} \quad (5b)$$

$$\eta_{xy} = p_M\eta_{xy,M} + p_D\eta_{xy,D} \quad (5c)$$

$$NOE = p_MNOE_M + p_DNOE_D \quad (5d)$$

where subscripts M and D indicate the monomeric and dimeric states, respectively. Here, R_{ex} includes intramolecular exchange in the monomeric and dimeric states, as well as exchange between monomeric and dimeric states. In general, the effects of multiple exchange processes are complex, and cannot be unraveled directly using the currently available data. If R_{ex} is negligible, then equation (5) can be written in the form:

$$R/p_M = R_M + R_D p_D/p_M \quad (6)$$

where R represents any of the relaxation rates of equation (5). By measuring the relaxation rates at several well-determined populations, p_D and p_M , the rates of the monomeric and dimeric states can be extracted as the intercept and slope from linear regression of R/p_M versus p_D/p_M .

Identification of exchange processes

R_{ex} may be estimated from the relationship:

$$R_{ex} = R_2 - \eta_{xy} \frac{\sqrt{3}(3D^2 + 4C^2)}{12CDP_2(\cos \beta)} \quad (7)$$

in which $D = \mu_0 h \gamma_H \gamma_N \langle r_{NH}^{-3} \rangle / (8\pi^2)$ and $C = \gamma_N B_0 \Delta\sigma / \sqrt{3}$, μ_0 is the permeability of free space, h is Planck's constant, γ_H and γ_N are the gyromagnetic ratios of 1H and ^{15}N , respectively, $\langle r_{NH}^{-3} \rangle^{-1/3} = 1.02 \text{ \AA}$ is the effective nitrogen–hydrogen bond length, $B_0 = 14.1 \text{ T}$ is the static magnetic field strength, $\Delta\sigma = -172(\pm 5.5) \text{ ppm}$ ⁵⁸ is the anisotropy of the (assumed) axially symmetric chemical shielding tensor of the backbone ^{15}N nucleus, and $\beta = 15(\pm 7)^\circ$ ⁶⁴ is the angle between the unique principal axis of the chemical shielding tensor and the N–H bond vector, and $P_2(x) = (3x^2 - 1)/2$. In the case of the indole $^{15}N^{e1}$ of tryptophan, the shielding tensor is significantly asymmetric.⁶⁵ The qualitative interpretation of exchange employed in this work for the indole $^{15}N^{e1}$ spin does not require that asymmetry is correctly accounted for. Thus, equation (7) was used also for tryptophan side-chains to yield apparent exchange rates that are reported in Figure 7(b). Contributions from the spectral density function at high frequencies, $\sim J(\omega_H)$, have been neglected in equation (7), since these are approximately two orders of magnitude smaller than the leading terms. Error propagation of β and σ yields $R_{ex} = R_2 - (1.3 \pm 0.1)\eta_{xy}$ in the case of backbone nuclei.

In the case of fast two-state exchange between monomers and dimers, R_{ex} can be approximated as:⁶⁶

$$R_{\text{ex}} = \frac{p_M p_D (\delta\omega)^2}{k_{\text{ex}}} \left(1 - \frac{2}{k_{\text{ex}} \tau_{\text{cp}}} \tanh \left[\frac{k_{\text{ex}} \tau_{\text{cp}}}{2} \right] \right) \quad (8)$$

where p_M and p_D indicate the populations of the monomer and dimer, respectively, $\delta\omega$ is the chemical shift difference between the two states, τ_{cp} is the delay between refocusing pulses in the CPMG sequence. The microscopic exchange rate is given by:

$$k_{\text{ex}} = k_{\text{off}} + k_{\text{on}}[M] = k_{\text{off}}(1 + p_M c / K_d) \quad (9)$$

Inserting this expression into equation (8), together with p_M as defined by equations (3) and (4), monomer–dimer exchange can be expressed as a function of k_{off} , K_d , and c . Given the value of K_d determined here, R_{ex} is an increasing function of c over the entire concentration range monitored here, irrespective of k_{off} and $\delta\omega$ (identical results are obtained using the full expression for two-state exchange^{67,68}). In reality, a given residue may experience a combination of intermolecular and intramolecular exchange, resulting in a complex pattern of R_{ex} as a function of concentration.

Rotational diffusion analysis

Rotational diffusion was analyzed using R_2/R_1 values from 46 residues in well-ordered secondary structure elements with NOE > 0.7 and $R_2/\eta_{xy} < 1.4$ at all three concentrations for which η_{xy} had been measured. The crystal structures of the monomeric wild-type protein (1PNT¹⁶) and the dimeric S19A mutant (1C0E¹⁸) were protonated using Molmol.⁶⁹ Optimization of the rotational diffusion tensor against the experimental data was performed using TENSOR version 2.0.⁷⁰ Selection between models with different numbers of parameters was performed using F -statistical testing,⁴¹ and the statistical significance of the test statistics was determined by the p -value, which states the probability that the observed value of the test statistic would be equalled or exceeded by random chance. For $p \leq \alpha$, the test statistic is significant at the $(1 - \alpha)\%$ confidence level. p -Values were obtained from the F -ratio distribution, as implemented in Mathematica (Wolfram Research). Hydrodynamic calculations were performed using HYDRONMR version 5.0a⁴⁴ with an atomic element radius of 3.3 Å, which has been shown to yield good agreement with the experimental values for a large set of proteins.⁷¹

Model-free analysis

Five different motional models with up to three parameters describing the internal motions of the system were used:⁷² (1) $S^2 = S_f^2$, $\tau_f = 0$, leaving S^2 to be optimized; (2) $S^2 = S_f^2$, leaving S^2 and τ_e to be optimized; (3) and (4) identical to (1) and (2), but with the addition of R_{ex} to account for μs – ms time scale motions; and (5) $\tau_f = 0$, leaving S^2 , S_f^2 and τ_e to be optimized. Model-free optimizations were performed using TENSOR version 2.0.⁷⁰ Model selection relied on extensive F -statistical testing (see above), as implemented in TENSOR. Standard errors in the estimated model-free parameters were obtained from Monte Carlo simulations using 500 samples.³¹

Acknowledgments

This research was supported by a grant from the Swedish Research Council awarded to M.A. R.L.V.E. was supported by US DHHS grant GM27003. T.Å. holds a predoctoral fellowship from the Structural Biology Network of the Swedish Foundation for Strategic Research. We thank Simona Mirón for assistance with recording the NOESY-HSQC experiment, Kristofer Modig for the Matlab routines for non-linear optimization, and Kristina Zachrisson for amino acid composition analysis. Ming-Ming Zhou kindly provided chemical shift assignments of LMW-PTP at 37 °C.

References

- Hunter, T. (1995). Protein kinases and phosphatases: the Yin and Yang of protein phosphorylation and signaling. *Cell*, **80**, 225–236.
- Tonks, N. K. & Neel, B. G. (1996). From form to function: signaling by protein tyrosine phosphatases. *Cell*, **87**, 365–368.
- Heinrikson, R. L. (1969). Purification and characterization of a low molecular weight acid phosphatase from bovine liver. *J. Biol. Chem.* **244**, 299–307.
- Waheed, A., Laidler, P. M., Wo, Y. Y. & Van Etten, R. L. (1988). Purification and physicochemical characterization of a human placental acid phosphatase possessing phosphotyrosyl protein phosphatase activity. *Biochemistry*, **27**, 4265–4273.
- Barford, D., Jia, Z. & Tonks, N. A. (1995). Protein tyrosine phosphatases take off. *Nature Struct. Biol.* **2**, 1043–1053.
- Zhang, Z. Y. (1998). Protein-tyrosine phosphatases: biological function, structural characteristics, and mechanism of catalysis. *Crit. Rev. Biochem. Mol. Biol.* **33**, 1–52.
- Stuckey, J. A., Schubert, H. L., Fauman, E., Zhang, Z.-Y., Dixon, J. E. & Saper, M. A. (1994). Crystal structure of Yersinia protein tyrosine phosphatase at 2.5 Å and the complex with tungstate. *Nature*, **370**, 571–575.
- Schubert, H. L., Fauman, E. B., Stuckey, J. A., Dixon, J. E. & Saper, M. A. (1995). A ligand-induced conformational change in the Yersinia protein tyrosine phosphatase. *Protein Sci.* **4**, 1904–1913.
- Jia, Z., Barford, D., Flint, A. J. & Tonks, N. K. (1995). Structural basis for phosphotyrosine peptide recognition by protein tyrosine phosphatase 1B. *Science*, **268**, 1754–1758.
- Wang, S., Tabernero, L., Zhang, M., Harms, E., Van Etten, R. L. & Stauffacher, C. V. (2000). Crystal structures of a low-molecular weight protein tyrosine phosphatase from *Saccharomyces cerevisiae* and its complex with the substrate *p*-nitrophenyl phosphate. *Biochemistry*, **39**, 1903–1914.
- Wang, F., Li, W., Emmett, M. R., Hendrickson, C. L., Marshall, A. G., Zhang, Y.-L., Wu, L. & Zhang, Z.-Y. (1998). Conformational and dynamic changes in Yersinia protein tyrosine phosphatase induced by ligand binding and active site mutation and revealed by H/D exchange and electrospray ionization Fourier transform ion cyclotron resonance mass spectrometry. *Biochemistry*, **37**, 15289–15299.
- Juszcak, L. J., Zhang, Z.-Y., Wu, L., Gottfried, D. S. & Eads, D. D. (1997). Rapid loop dynamics of Yersinia protein tyrosine phosphatase. *Biochemistry*, **36**, 2227–2236.
- Logan, T. M., Zhou, M.-M., Nettesheim, D. G., Meadows, R. P., Van Etten, R. L. & Fesik, S. W.

- (1994). Solution structure of a low molecular weight protein tyrosine phosphatase. *Biochemistry*, **33**, 11087–11096.
14. Zhang, Z.-Y. & Van Etten, R. L. (1991). Pre-steady-state and steady-state kinetics of the low molecular weight phosphotyrosyl protein phosphatase from bovine heart. *J. Biol. Chem.* **266**, 1516–1525.
15. Zhang, Z. Y. & Van Etten, R. L. (1990). Purification and characterization of a low-molecular-weight acid phosphatase—a phosphotyrosyl-protein phosphatase from bovine heart. *Arch. Biochem. Biophys.* **282**, 39–49.
16. Zhang, M., Van Etten, R. L. & Stauffacher, C. V. (1994). Crystal structure of bovine heart phosphotyrosyl phosphatase at 2.2 Å resolution. *Biochemistry*, **33**, 11097–11105.
17. Zhang, M., Zhou, M.-M., Van Etten, R. L. & Stauffacher, C. V. (1997). Crystal structure of bovine low molecular weight phosphotyrosyl phosphatase complexed with the transition state analog vanadate. *Biochemistry*, **36**, 15–23.
18. Taberner, L., Evans, B. N., Tishmack, P. A., Van Etten, R. L. & Stauffacher, C. V. (1999). The structure of the bovine protein tyrosine phosphatase dimer reveals a potential self-regulation mechanism. *Biochemistry*, **38**, 11651–11658.
19. Tailor, P., Gilman, J., Williams, S., Couture, C. & Mustelin, T. (1997). Regulation of the low molecular weight phosphotyrosine phosphatase by phosphorylation at tyrosines 131 and 132. *J. Biol. Chem.* **272**, 5371–5374.
20. Rigacci, S., Degl'Innocenti, D., Bucciantini, M., Cirri, P., Berti, A. & Ramponi, G. (1996). pp60v-src phosphorylates and activates low molecular weight phosphotyrosine-protein phosphatase. *J. Biol. Chem.* **271**, 1278–1281.
21. Stein, E., Lane, A. A., Cerretti, D. P., Schoecklmann, H. O., Schroff, A. D., Van Etten, R. L. & Daniel, T. O. (1998). Eph receptors discriminate specific ligand oligomers to determine alternative signaling complexes, attachment, and assembly responses. *Genes Dev.* **12**, 667–678.
22. Ellis, R. J. (2001). Macromolecular crowding: and important but neglected aspect of the intracellular environment. *Curr. Opin. Struct. Biol.* **11**, 114–119.
23. Cirri, P., Fiaschi, T., Chiarugi, P., Camici, G., Manao, G., Rauegi, G. & Ramponi, G. (1996). The molecular basis of the differing kinetic behaviour of the two low molecular mass phosphotyrosine protein phosphatase isoforms. *J. Biol. Chem.* **271**, 2604–2607.
24. Zhang, M., Stauffacher, C. V., Lin, D. & Van Etten, R. L. (1998). Crystal structure of a human low molecular weight phosphotyrosyl phosphatase. Implications for substrate specificity. *J. Biol. Chem.* **273**, 21714–21720.
25. Zhang, Z., Harms, E. & Van Etten, R. L. (1994). Asp129 of low molecular weight protein tyrosine phosphatase is involved in leaving group protonation. *J. Biol. Chem.* **269**, 25947–25950.
26. Chiarugi, P., Cirri, P., Marra, F., Rauegi, G., Camici, G., Manao, G. & Ramponi, G. (1997). LMW-PTP is a negative regulator of insulin-mediated mitotic and metabolic signaling. *Biochem. Biophys. Res. Commun.* **238**, 676–682.
27. Wo, Y.-Y. P., McCormack, A. L., Shabanowitz, J., Hunt, D. F., Davis, J. P., Mitchell, G. L. & Van Etten, R. L. (1992). Sequencing, cloning and expression of human red cell-type acid phosphatase, a cytoplasmic phosphotyrosyl protein phosphatase. *J. Biol. Chem.* **267**, 10856–10865.
28. Ramponi, G. & Stefani, M. (1997). Structural, catalytic, and functional properties of low Mr, phosphotyrosine protein phosphatases. Evidence of a long evolutionary history. *Int. J. Biochem. Cell. Biol.* **29**, 279–292.
29. Zhou, M.-M., Logan, T. M., Thèriault, Y., Van Etten, R. L. & Fesik, S. W. (1994). Backbone ^1H , ^{13}C , and ^{15}N assignments and secondary structure of bovine low molecular weight phosphotyrosyl protein phosphatase. *Biochemistry*, **1994**, 5221–5229.
30. Pfuhl, M., Chen, H. A., Kristensen, S. M. & Driscoll, P. C. (1999). NMR exchange broadening arising from specific low affinity protein self-association: analysis of nitrogen-15 nuclear relaxation for rat CD2 domain 1. *J. Biomol. NMR*, **14**, 307–320.
31. Press, W. H., Flannery, B. P., Teukolsky, S. A. & Vetterling, W. T. (1986). *Numerical Recipes. The Art of Scientific Computing*, Cambridge University Press, Cambridge.
32. Fushman, D., Cahill, S. & Cowburn, D. (1997). The main-chain dynamics of the dynamin pleckstrin homology (PH) domain in solution: analysis of ^{15}N relaxation with monomer/dimer equilibration. *J. Mol. Biol.* **266**, 173–194.
33. Mercier, P., Spyropoulos, L. & Sykes, B. D. (2001). Structure, dynamics, and thermodynamics of the structural domain of troponin C in complex with the regulatory peptide 1–40 of troponin I. *Biochemistry*, **40**, 10063–10077.
34. Korchuganov, D. S., Nolde, S. B., Reibarkh, M. Y., Orekhov, V. Y., Schulga, A. A., Ermolyuk, Y. S. *et al.* (2001). NMR study of monomer–dimer equilibrium of barstar in solution. *J. Am. Chem. Soc.* **123**, 2068–2069.
35. Le, H. & Oldfield, E. (1994). Correlation between ^{15}N NMR chemical shifts in proteins and secondary structure. *J. Biomol. NMR*, **4**, 341–348.
36. de Dios, A. C., Pearson, J. G. & Oldfield, E. (1993). Secondary and tertiary structural effects on protein NMR chemical shifts: an *ab initio* approach. *Science*, **260**, 1491–1496.
37. Wang, L., Pang, Y., Holder, T., Brender, J. R., Kurochkin, A. V. & Zuiderweg, E. R. P. (2001). Functional dynamics in the active site of the ribonuclease binase. *Proc. Natl Acad. Sci. USA*, **98**, 7684–7689.
38. Su, X. D., Taddei, N., Stefani, M., Ramponi, G. & Nordlund, P. (1994). The crystal structure of a low-molecular-weight phosphotyrosine protein phosphatase. *Nature*, **370**, 575–578.
39. Kolmodin, K. & Aqvist, J. (1999). Computational modeling of catalysis and binding in low-molecular-weight protein tyrosine phosphatase. *Int. J. Quant. Chem.* **73**, 147–159.
40. Northrup, S. H. & Erickson, H. P. (1992). Kinetics of protein–protein association explained by Brownian dynamics computer simulation. *Proc. Natl Acad. Sci. USA*, **89**, 3338–3342.
41. Devore, J. (1982). *Probability and Statistics for Engineering and the Sciences*, Brooks/Cole Publishing Company, Monterey.
42. Lee, L. K., Rance, M., Chazin, W. J. & Palmer, A. G. (1997). Rotational diffusion anisotropy of proteins from simultaneous analysis of ^{15}N and ^{13}C nuclear spin relaxation. *J. Biomol. NMR*, **9**, 287–298.
43. Cavanagh, J., Fairbrother, W. J., Palmer, A. G. & Skelton, N. J. (1995). *Protein NMR Spectroscopy: Principles and Practice*, Academic Press, San Diego.
44. Garcia de la Torre, J., Huertas, M. L. & Carrasco, B. (2000). HYDRONMR: prediction of NMR relaxation

- of globular proteins from atomic-level structures and hydrodynamic calculations. *J. Magn. Reson.* **147**, 138–146.
45. Krishnan, V. V. & Cosman, M. (1998). An empirical relationship between rotational correlation time and solvent accessible surface area. *J. Biomol. NMR*, **12**, 177–182.
 46. Ottiger, M., Zerbe, O., Guntert, P. & Wuthrich, K. (1997). The NMR solution conformation of unligated human cyclophilin A. *J. Mol. Biol.* **272**, 64–81.
 47. Cantor, R. C. & Schimmel, P. R. (1980). *Biophysical Chemistry, II*, W.H. Freeman, San Francisco.
 48. Goodman, J. L., Pagel, M. D. & Stone, M. J. (2000). Relationships between protein structure and dynamics from a database of NMR-derived backbone order parameters. *J. Mol. Biol.* **295**, 963–978.
 49. Epstein, D. M., Benkovic, S. J. & Wright, P. E. (1995). Dynamics of the dihydrofolate reductase–folate complex: catalytic sites and regions known to undergo conformational change exhibit diverse dynamical features. *Biochemistry*, **34**, 11037–11048.
 50. Stone, M. J., Fairbrother, W. J., Palmer, A. G., Reizer, J., Saier, M. H. & Wright, P. E. (1992). The backbone dynamics of the *Bacillus subtilis* glucose permease IIA domain determined from ^{15}N NMR relaxation measurements. *Biochemistry*, **31**, 4394–4406.
 51. Schurr, J. M., Babcock, H. P. & Fujimoto, B. S. (1994). A test of the model-free formulas. Effects of anisotropic rotational diffusion and dimerization. *J. Magn. Reson. ser. B*, **105**, 211–224.
 52. Wo, Y.-Y. P., Zhou, M.-M., Stevis, P., Davis, J. P., Zhang, Z.-Y. & Van Etten, R. L. (1992). Cloning, expression, and catalytic mechanism of the low molecular weight phosphotyrosyl protein phosphatase from bovine heart. *Biochemistry*, **31**, 1712–1721.
 53. Norwood, T. J., Boyd, J. E., Heritage, J. E., Soffe, N. & Campbell, I. D. (1990). Comparison of techniques for ^1H -detected heteronuclear ^1H – ^{15}N spectroscopy. *J. Magn. Reson.* **87**, 488–501.
 54. Bax, A., Ikura, M., Kay, L. E., Torchia, D. A. & Tschudin, R. (1990). Comparison of different modes of two-dimensional reverse-correlation NMR for the study of proteins. *J. Magn. Reson.* **86**, 304–318.
 55. Kay, L. E., Torchia, D. A. & Bax, A. (1989). Backbone dynamics of proteins as studied by nitrogen-15 inverse detected heteronuclear NMR spectroscopy: application to staphylococcal nuclease. *Biochemistry*, **28**, 8972–8979.
 56. Kördel, J., Skelton, N. J., Akke, M., Palmer, A. G. & Chazin, W. J. (1992). Backbone dynamics of calcium-loaded calbindin D_{9k} studied by two-dimensional proton-detected NMR spectroscopy. *Biochemistry*, **31**, 4856–4866.
 57. Tjandra, N., Szabo, A. & Bax, A. (1996). Protein backbone dynamics and ^{15}N chemical shift anisotropy from quantitative measurement of relaxation interference effects. *J. Am. Chem. Soc.* **118**, 6986–6991.
 58. Kroenke, C. D., Loria, J. P., Lee, L. K., Rance, M. & Palmer, A. G. (1998). Longitudinal and transverse ^1H – ^{15}N dipolar/ ^{15}N chemical shift anisotropy relaxation interference: unambiguous determination of rotational diffusion tensors and chemical exchange effects in biological macromolecules. *J. Am. Chem. Soc.* **120**, 7905–7915.
 59. Farrow, N. A., Muhandiram, R., Singer, A. U., Pascal, S. M., Kay, C. M., Gish, G. *et al.* (1994). Backbone dynamics of a free and phosphopeptide-complexed Src homology 2 domain studied by ^{15}N NMR relaxation. *Biochemistry*, **33**, 5984–6003.
 60. Delaglio, F., Grzesiek, S., Vuister, G. W., Zhu, G., Pfeifer, J. & Bax, A. (1995). NMRPipe: a multi-dimensional spectral processing system based on UNIX pipes. *J. Biomol. NMR*, **6**, 277–293.
 61. Johnson, B. A. & Blevins, R. A. (1994). NMRView: a computer program for the visualization and analysis of NMR data. *J. Biomol. NMR*, **4**, 603–614.
 62. Palmer, A. G., Rance, M. & Wright, P. E. (1991). Intramolecular motions of a zinc finger DNA-binding domain from xfin characterized by proton-detected natural abundance ^{13}C heteronuclear NMR spectroscopy. *J. Am. Chem. Soc.* **113**, 4371–4380.
 63. Wennerström, H. (1972). Nuclear magnetic relaxation induced by chemical exchange. *Mol. Phys.* **24**, 69–80.
 64. Fushman, D., Tjandra, N. & Cowburn, D. (1998). Direct measurement of ^{15}N chemical shift anisotropy in solution. *J. Am. Chem. Soc.* **120**, 10947–10952.
 65. Ramamoorthy, A., Wu, C. H. & Opella, S. J. (1997). Magnitudes and orientations of the principal elements of the ^1H chemical shift ^1H – ^{15}N dipolar coupling, and ^{15}N chemical shift interaction tensors in $^{15}\text{N}_{\epsilon 1}$ -tryptophan and $^{15}\text{N}_{\pi}$ -histidine side chains determined by three-dimensional solid-state NMR spectroscopy and polycrystalline samples. *J. Am. Chem. Soc.* **119**, 10479–10486.
 66. Luz, Z. & Meiboom, S. (1963). Nuclear magnetic resonance study of the protolysis of trimethylammonium ion in aqueous solution—order of the reaction with respect to solvent. *J. Chem. Phys.* **39**, 366–370.
 67. Davis, D. G., Perlman, M. E. & London, R. E. (1994). Direct measurements of the dissociation-rate constant for inhibitor–enzyme complexes *via* the $\text{T}_{1\rho}$ and T_2 (CPMG) methods. *J. Magn. Reson. ser. B*, **104**, 266–275.
 68. Carver, J. P. & Richards, R. E. (1972). A general two-site solution for the chemical exchange produced dependence of T_2 upon the Carr–Purcell pulse separation. *J. Magn. Reson.* **6**, 89–105.
 69. Koradi, R., Billeter, M. & Wüthrich, K. (1996). MOLMOL: a program for display and analysis of macromolecular structures. *J. Mol. Graph.* **14**, 51–55.
 70. Dosset, P., Hus, J.-C., Blackledge, M. & Marion, D. (2000). Efficient analysis of macromolecular rotational diffusion from heteronuclear relaxation data. *J. Biomol. NMR*, **16**, 23–28.
 71. Bernado, P., Garcia de la Torre, J. & Pons, M. (2002). Interpretation of ^{15}N NMR relaxation data of globular proteins using hydrodynamic calculations with HYDRONMR. *J. Biomol. NMR*, **23**, 139–150.
 72. Mandel, A. M., Akke, M. & Palmer, A. G. (1995). Backbone dynamics of *Escherichia coli* ribonuclease HI: correlations with structure and function in an active enzyme. *J. Mol. Biol.* **246**, 144–163.

Edited by P. E. Wright

(Received 11 March 2002; received in revised form 8 July 2002; accepted 9 July 2002)